

Optimisation of hydraulic fracturing parameters based on cohesive zone method in oil shale reservoir with random distribution of weak planes

Lianghao Zhai^{a,b}, Han Zhang^{a,b}, Dongbin Pan^{a,b}, Ying Zhu^{a,b}, Jiang Zhu^{a,b}, Ying Zhang^{a,b}, Chen Chen^{a,b,*}

^a College of Construction Engineering, Jilin University, Changchun, 130026, China

^b Key Laboratory of Drilling and Exploitation Technology in Complex Conditions, Ministry of Natural Resources, Changchun, 130026, China

ARTICLE INFO

Keywords:

Hydraulic fracturing technology
Oil shale
Cohesive zone method
Orthogonal test
Fracture propagation

ABSTRACT

Hydraulic fracturing technology plays a key role in the in-situ exploitation of oil shale. A mechanism for generating complex fracture networks in oil shale reservoirs with randomly distribution weak planes is of vital importance to hydraulic fracturing design. In this study, the cohesive zone method (CZM) was adopted to establish a reservoir model with randomly distributed weak planes. Furthermore, the concept of “reservoir reconstruction efficiency (RRE)” was proposed as an index to evaluate the results of hydraulic fracturing. Using the proposed model and orthogonal test, we found that the flow rate has the most significant influence on the RRE, followed by the perforation direction and perforation length. For the simulated reservoir, a flow rate of 0.008 m³/s and perforation direction consistent with the maximum principal stress were the optimal fracturing parameters. Moreover, numerous radial branch fractures were generated under extremely high flow rate. The findings of this study are expected to provide significant help in predicting the fracture propagation and optimising the fracture parameters in oil shale exploitation.

1. Introduction

The energy crisis, which is a consequence of the rapid development of the global economy, has become acritical issue that requires immediate attention. Oil shale, which is regarded as an important alternative source of oil, is widely distributed worldwide (OTS, 2005). The development modes of oil shale can be mainly classified into ground retorting and *in situ* thermal conversion. Ground retorting of oil shale results in environmental pollution. Moreover, it is difficult to develop oil shale resources in deep areas using this method (Kang et al., 2011; Väizene et al., 2016). Therefore, *in situ* conversion technology, as a method for the development of oil shale resources, has been attracting the attention of researchers over the world in recent years (Sun et al., 2012; Zhao et al., 2019). However, the permeability, porosity, and thermal conductivity of oil shale are extremely low and hinder the heat transfer from the heat injection wells to the reservoir, as well as the migration of pyrolysis products to the production wells (Guo et al., 2013; Nagel et al., 2013; Yang Hao, 2014). Consequently, oil shale reservoirs must be reconstructed using hydraulic fracturing technology to realise their

commercial exploitation. Researchers from Jilin University, China have carried out *in-situ* oil shale hydraulic fracturing and heat injection exploitation in the Fuyu and Nong'an pilot demonstration project and obtained excellent experimental results. It was found that the natural fractures could be reactivated through stimulation, thereby changing the extension paths of the hydraulic fractures (Gale et al., 2007). In addition, the outcrops, cores and image logs were studied, and it was found that the weak planes (i.e., the natural fractures and bedding planes) were common in shale, however, the potential importance of weak planes had rarely been studied (Gale et al., 2014). In another study, it was inferred that natural fractures were commonly present in unconventional reservoirs (Xie et al., 2018b). Furthermore, it was observed that different fracturing parameters would lead to different extension behaviours. Therefore, the influence of weak planes cannot be ignored while predicting the extension behaviour of hydraulic fractures and optimising the fracturing parameters.

Research on hydraulic fracturing has been carried out for several decades. The extension process of hydraulic fractures in coal was studied using an acoustic emission system (Liang et al., 2017). In the same year,

* Corresponding author. College of Construction Engineering, Jilin University, China.

E-mail addresses: dilh17@mails.jlu.edu.cn (L. Zhai), hanz16@mails.jlu.edu.cn (H. Zhang), pandb16@mails.jlu.edu.cn (D. Pan), yingzhu18@mails.jlu.edu.cn (Y. Zhu), jiangzhu16@mails.jlu.edu.cn (J. Zhu), yingzhang17@mails.jlu.edu.cn (Y. Zhang), chenchen@jlu.edu.cn (C. Chen).

<https://doi.org/10.1016/j.jngse.2019.103130>

Received 30 April 2019; Received in revised form 13 November 2019; Accepted 23 December 2019

Available online 8 January 2020

1875-5100/© 2019 Elsevier B.V. All rights reserved.

the influence of natural fractures on the extension of hydraulic fractures was analysed in coal seams (Wang et al., 2017). The propagation behaviour of hydraulic fractures under the influence of natural fractures was studied by some researchers by inserting printer paper into cement blocks in fracturing tests (Cheng et al., 2015b; Dehghan et al., 2015; Zhou et al., 2008). In addition, an innovative method of heating and cooling cycling was introduced to study the influence of natural fractures with a random distribution (Zhou et al., 2010). Some researchers have studied the fracturing parameters to optimise the hydraulic fractures. Bing performed an experiment to determine the optimum conditions that promote the formation of fracture network (Bing et al., 2014). Subsequently, a 3D fracture propagation model was established to study the influence of various cluster spaces on the propagation of hydraulic fractures, and to determine the optimal condition (Guo et al., 2015a). In summary, these studies have greatly improved our knowledge of the extension of hydraulic fractures under the influence of natural fractures. However, experimental samples cannot accurately simulate the *in-situ* situation. Accordingly, many scholars prefer to use numerical simulation methods, which makes the research process more convenient and flexible.

At present, the numerical simulation of hydraulic fracturing networks mainly involves the following four methods: (1) Displacement discontinuity method (DDM): Here, the Mohr-Coulomb friction was used to investigate the physical activation of natural fractures under the action of pressurised hydraulic fractures (Chuprakov et al., 2011). The DDM can also be used to simulate the process of rock fracturing and study the intersections between a hydraulic fracture and a pre-existing fracture (Xie et al., 2016). Many scholars have already recognised that DDM can handle the extension problem of complex fractures. However, it is difficult to simulate the extension of fractures in heterogeneous materials and achieve fluid-solid coupling between the rock matrix and the fractures with this method. (2) Distinct Element Method (DEM): The extension behaviour of hydraulic fractures under the influence of natural fractures was studied using the DEM, and the validity of this method was verified through experimental studies (Fatahi et al., 2017). In a related study, the DEM was used to investigate the behaviour near a wellbore considering the effect of pre-existing defects and the influence of far field stress (AbuAisha et al., 2017). In addition, the discontinuous deformation analysis (DDA) method can also be used to simulate the hydraulic fracturing process. The physical behaviour of stress-deformation and fluid flow in fractures was studied using DDA (Jing et al., 2001). Employing DDA blocks with finite element meshes, a hydro-mechanical analysis algorithm was introduced to determine the hydraulic fracture initiation and its propagation (Choo et al., 2016). In summary, the DEM blocks are used to represent the rock mass, which means that the contact stiffness and strength parameters between the elements must be calculated continuously, especially for discontinuous surfaces. In view of these reasons, the simulation of this method involves a large number of calculations. (3) Extended Finite Element Method (XFEM): In this method, discontinuous enrichment functions are added to the conventional finite element method. Therefore, the fracture extension is not limited to the boundaries of the meshes. The XFEM can achieve a high precision in simulating the extension behaviour of fractures and the competitive extension of multiple fractures (Belytschko and Black, 1999). The propagation of hydraulic fractures and the characteristics of orthogonal anisotropy of shales were also studied using the XFEM (Wang et al., 2016). An upwind scheme was introduced in the XFEM to evaluate the transportation and distribution of the proppant in fractures (Shi et al., 2016). However, this method is not convenient for dealing with the intersection and bifurcation behaviour of hydraulic fractures. The limitations of this method will be expanded when focusing on the effects of multiple weak planes, such as natural fractures and bedding planes. (4) Finite Element Method (FEM): Numerous scholars have carried out significant hydraulic fracturing work on various types of rocks using the finite element method. The cohesive zone method (CZM) based on a viscoelastic-plastic-damage

constitutive model has been increasingly applied to the simulation of hydraulic fracturing. The hydraulic fracturing process and the interaction of hydraulic fractures with natural fractures were successfully simulated and different fracture mechanisms were studied using the CZM (Dahi Taleghani et al., 2016). The fluid-solid coupling process and the initiation and propagation of hydraulic fractures could be simulated by using a standard time integration algorithm and selecting special element types with intermediate seepage nodes. Based on the CZM, the initiation and propagation of fractures were studied under different geological and fracturing parameters (Guo et al., 2017). A finite element model considering the pore pressure was established to investigate the propagation of fractures under different cohesive parameters and fluid viscosities (Chen et al., 2009). Combined with a poroelastic-based model, the CZM was used to study the influence of geological factors and stress shadow on the propagation of fractures (Bryant et al., 2015). Furthermore, based on this method, a zero-thickness finite element was developed to model the fracture propagation (Carrier and Granet, 2012). A 3D pore pressure CZM was established to study the nucleation and propagation of hydraulic fractures (Yao et al., 2015). The stress-seepage-damage field was coupled on the basis of the CZM to simulate the interaction between a hydraulic fracture and a single natural fracture under different conditions (Guo et al., 2015b). The influence of natural fractures on hydraulic fracture propagation and sensitivity analysis of the main parameters was studied (Taleghani et al., 2018). A combined numerical and experimental method was used to assess the verification and validation of cohesive finite element models in simulating a dynamic fracture along weak planes (Arias et al., 2007). Furthermore, the cohesive law framework was used to study the propagation behaviour of intra-laminar fractures in composite materials (Wu et al., 2013). However, for this method, the fracture extension path must be set in advance during the modelling and thus, the random extension of fractures cannot be accurately realised. However, the CZM still has the following advantages: **a.** the intersection and bifurcation behaviour of fractures can be handled without introducing complex shape-functions; **b.** the fluid-solid coupling between the rock matrix and the fractures can be effectively realised with this method; **c.** materials with heterogeneous and complex constitutive relationships can be conveniently defined; **d.** both stress and pressure singularities at the tip of the fracture can be avoided.

In the model proposed in this study, stress-seepage-damage field coupling is used to simulate the deformation of the oil shale matrix and the liquid exchange based on the CZM. Instead of prefabricating the extension paths of the fractures, the Python programming language was used to handle the nodes in the model and a layer of zero thickness cohesive elements were added around the boundaries of all the meshes within the model. In addition, a random function was used to insert random natural fractures into the model to simulate the *in-situ* reservoir status. As the main and branch fractures may be generated during the extension process of hydraulic fractures, the cumulative fracture length and the maximum fracture width were chosen as the evaluation indices of reservoir reconstruction efficiency (RRE). On this basis, orthogonal test was designed to determine the significant fracturing parameters among the flow rate of the fracturing fluid and the length and direction of the perforation. Subsequently, a single factor analysis was performed to investigate the extension of hydraulic fractures under the influence of the significant factors obtained from the results of the orthogonal test. The results show that the accuracy of predictions of the propagation behaviour of the fractures affected by weak planes could be improved and the fracturing parameters could be optimised to achieve a better RRE.

2. Model description

Based on Biot's fluid-solid coupling equation and the displacement-based damage evolution criterion, the intersection between the hydraulic and natural fractures was modelled using the CZM in this study.

The Python programming language and a random function were used to achieve the random distribution of natural fractures. The mesh nodes in the model area were processed to form a layer of zero thickness cohesive elements at the edge of all meshes without introducing pre-determined extension path. This model can be used to study the influence of a randomly distributed status of natural fractures on the propagation behaviour of hydraulic fractures. To simulate the fracture propagation and fluid flow during hydraulic fracturing in oil shale reservoirs fully, different types of elements were selected to represent the oil-shale matrix and the fracture system and different material properties were assigned to different parts of elements. Finally, fluid seepage through the porous medium and the elastic deformation of the rock matrix were coupled in this model to simulate the leakage of the fracturing fluid from the main fracture to the oil shale matrix and the natural fracture, as well as the transfer of pore pressure in the model.

The propagation of hydraulic fractures in natural fracture-developed reservoirs mainly includes the following four physical processes: (1) fracture initiation, (2) flow of the fracturing fluid in the fracture network, including the flow in the tangential direction inside the fracture and the flow in the normal direction into the rock matrix, (3) stimulation and extension of natural fractures and (4) deformation of the rock around the fracture under the action of the fracturing fluid.

2.1. Fundamental theory

Similar to other types of shale, oil shale can be treated as a porous medium. Therefore, the poro-elasticity theory can be used to explain the behaviour of oil shale during hydraulic fracturing. Because hydraulic fracturing is a typical fluid-solid coupling process, Biot's theory can be used to describe the deformation of the rock matrix and the dissipation of the pore fluid pressure. The opening and extension of fractures are represented by the opening and failure of cohesive elements embedded in the model.

2.1.1. Effective stress principle equation

Based on the effective stress principle, the coupling between the stress field of the rock matrix and the pressure field of the fluid can be obtained as follows:

$$\sigma_{total} = \sigma' + \alpha p_w \delta \quad (1)$$

where σ_{total} is the total stress; σ' is the tensor of the effective stress; α is the Biot coefficient; p_w is the pore pressure; and δ is the Kronecker constant.

2.1.2. Seepage equation

$$\frac{\nabla^2 P}{\mu(C_r + C_l)} = \frac{1}{K} \frac{\partial P}{\partial t} \quad (2)$$

where p is the pore pressure; μ is the viscosity of the fluid; ∇^2 is the Laplace operator; C_r is the rock compressibility coefficient; C_l is the fluid compressibility coefficient; t is the time; and K is the permeability of the rock.

2.1.3. Cohesive law

The cohesive law determines the relationship between the traction force on the probable fracture surface and the displacement of a cohesive element as shown in Fig. 1. In this study, we have adapted the irreversible bilinear cohesive law to simulate the failure of the element, as well as describe the fracture propagation behaviour.

Fig. 1 shows the damage-failure process of the cohesive element as the relative displacement of the fracture surface increases. To describe the damage behaviour of the element more accurately, a damage variable D is defined. The traction force linearly increases without the damage ($D = 0$) for all values of the displacement of the cohesive element less than U^0 . This damage-free state lasts until the linear

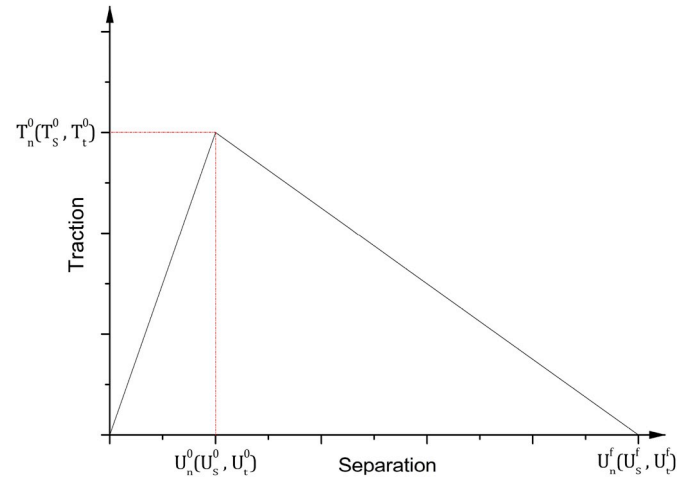


Fig. 1. Traction-separation law of the cohesive element.

increase in the traction reaches the maximum tensile strength T^0 and the corresponding displacement increases to U^0 . This displacement (U^0) also becomes the damage initiation displacement and the traction displacement curve is reversible. The linear reduction of the traction force is caused by the accumulation of damage in the material element owing to the continuous increase in the displacement. Finally, when the separation displacement reaches a specific value U^f , the cohesive element is destroyed completely (i.e., $D = 1$) and the corresponding traction force decreases to zero.

The maximum nominal stress traction-separation law is adopted here to measure the initiation of damage:

$$f = \left\{ \frac{\langle t_n \rangle}{t_n^0}, \frac{t_s}{t_s^0}, \frac{t_t}{t_t^0} \right\} \quad (3)$$

where t_n is the traction force along the normal direction of the possible fracture surface; $\langle t_n \rangle$ represents pure compression deformation; t_s and t_t represent the traction forces in the tangential direction, which are perpendicular to each other on the possible fracture surface; and t_n^0 , t_s^0 , and t_t^0 are the peak values of the nominal stress and the two traction forces in the shear direction, respectively. It is assumed the material begins to be damaged when $1.0 \leq f \leq 1.0 + f_{tol}$, wherein the default value of f_{tol} is 0.05. This means that the material enters the damage stage, irrespective of which stress in the three directions reaches its peak value in the corresponding direction.

When the displacement between the fractures exceeds U^0 , that is, the material enters the softening stage. The damage evolution criteria of the material must be defined to determine the degradation of the material stiffness. Based on the existing results of our research group, the displacement-based linear softening method has been chosen in this study to determine the damage evolution of materials (Shuai, 2017).

The damage variable of linear softening depicted in Fig. 1 can be determined as follows:

$$D = \frac{U_m^f (U_m^{max} - U_m^0)}{U_m^{max} (U_m^f - U_m^0)} \quad (4)$$

where U_m^0 is the effective displacement during the damage evolution; U_m^f is the displacement when the material fails; and U_m^{max} is the maximum effective displacement during the loading.

When the fracture propagation is simulated, it is assumed that the fluid inside the fracture is an incompressible Newtonian fluid. To simulate the propagation process of the hydraulic fracture fully, the tangential and normal flows of the fluid inside the fractures are considered as shown in Fig. 2.

The tangential fluid flow can be controlled by the lubrication equation.

$$q = -\frac{d^2}{12\mu} \nabla p \quad (5)$$

where q is the fluid flux of the tangential flow; d is the displacement of the fracture surface opening; ∇p is the fluid pressure gradient along the cohesive element; and μ is the viscosity of the fracturing fluid.

In addition to the tangential flow, a normal fluid flow occurs during fracturing due to the leakage of the fracture surface. To simulate the leakage of the fracturing fluid to the rock matrix, the properties of the cohesive element are set by defining the top and bottom fluid leakage coefficients, which allow the fluid pressure to interact with the cohesive element through the surrounding permeable material. All the mesh boundaries in the model are embedded into the cohesive elements with leakage coefficients to realise both the fluid leakage into the rock matrix and the transfer of pore pressure. The leakage of the fracturing fluid can be interpreted as the volume flow rate of the fluid flowing into an element in the simulation domain. The equations for calculating the normal flow of the fluid through the top and bottom surfaces of the failure element are as follows:

$$q_t = c_t (p_i - p_t) \quad (6)$$

$$q_b = c_b (p_i - p_b)$$

where q_t and q_b represent the volume flow rate of the top and bottom surfaces of the fracture element, respectively; c_t and c_b correspond to the leakage coefficients of the top and bottom surfaces, respectively; p_t and p_b are the pore pressures of the top and bottom surfaces in the adjacent elements, respectively; and p_i is the fluid pressure in the cohesive element that has been opened.

2.2. Model implementation

In this study, a two-dimensional (2D) hydraulic fracturing model was established by using the finite element analysis software ABAQUS. The following assumptions were made during modelling: (1) the fracture height was constant because of the 2D approximation; (2) the expansion of fractures under plane strain conditions was considered; and (3) the fracturing fluid was a Newtonian fluid. Based on the geological drilling evaluation data of the oil shale reservoirs in WangQing area, the thickness of the oil shale reservoir in this area is about 10 m. Therefore, the area of the model was 50 m*10 m as shown in Fig. 3. The parametric modelling with the Python language generates a random distribution of natural fractures and bedding planes in the model by means of the random function. Thus, an oil shale multiple media model containing natural fractures and bedding structures was generated and different material properties were assigned to each medium. The injection point

was built in the center of the model and the initial failure element was symmetrically set near the injection point. The length and direction of the initial failure element could be artificially adjusted to study the hydraulic fracturing effect under different perforation conditions.

In contrast to the earlier studies, which used the CZM to study the fracture propagation behaviour, the method proposed here had two significant differences and advantages. On the one hand, the cohesive elements are inserted at all mesh boundaries in this model. In the previous studies, various researchers focused on the interaction behaviour of a single hydraulic fracture and a single natural fracture under the influence of different geological and fracturing parameters. However, this may only represent a local interaction in the reservoir. The extended path of the fracture needs to be strictly planned in advance, and the fractures does not continue to propagate after the hydraulic crack reaches the boundary of the planned path. The hydraulic fractures can extend more freely to any position in our model. Furthermore, we focus on the extension of the entire hydraulic fractures within the reservoir model, which is more practical than the previous model. In addition, the weak planes in the current model have random occurrences and distributions. The CZM is often used to study the intersection among the fractures. Many researchers focused only on the effects of a single weak plane on the extension behaviour of the hydraulic fractures, while other studies paid attention to the influence of multiple weak planes with an orthogonal status. Moreover, some studies used models that had a series of mutually orthogonal weak planes. It is undeniable that all these studies have promoted the understanding of the intersection of hydraulic fractures and the weak planes. However, the distribution of weak planes in an actual reservoir is much more complicated than assumed in these studies. The weak planes with random occurrences and distributions in the current model in this study are much closer to the true state of the reservoirs than those in the previous models. Thus, it can simulate the extension of hydraulic fractures under the influence of multiple weak planes more accurately. To achieve fluid-solid coupling during the fracturing process, mass balance and fluid flow continuity at the intersection point must be ensured when operating the nodes. A crucial technique for this step is to merge the seepage nodes in the middle of the cohesive elements. The stress and seepage field of the cohesive element are changed by injecting the fracturing fluid according to the flow rate at the injection point. The damage and failure of the cohesive element during the continuous injection of the fracturing fluid are calculated based on a previously established constitutive relation. The cohesive elements that reach the failure condition are opened and connected to each other, and the hydraulic fracture network can be realised finally.

The oil shale matrix in this model adopts a four-node bilinear displacement and pore pressure element. This type of element can be used to simulate the deformation of rock matrix and permeation of fracturing fluid in fractures. A six-node displacement and 2D pore pressure cohesive element is used at the boundary of the oil shale matrix, natural fracture and bedding surface. The two nodes in the middle of the six-nodes of this element boundary are the seepage nodes. This type of cohesive element can simulate the fracture propagation, flow of the fracturing fluid within the fracture and the leakage of the fracturing fluid into the rock matrix. Because the simulated oil shale reservoir has a buried depth of 200 m, a pore water pressure of 2 MPa is prescribed in the whole model. The fixed boundary conditions are predefined in the X- and Y- directions.

2.3. Model input data

The data used for the simulation are shown in Table 1. Different material properties for the rock matrix, natural fracture and bedding planes were set to simulate the multi-media structure of the oil shale reservoir. We chose relatively low rock mechanical and failure parameters for the natural fracture and bedding plane to distinguish the three kinds of media. All data used in the simulation was obtained from the doctoral thesis of a graduated senior fellow in the research group (Gao, 2017).

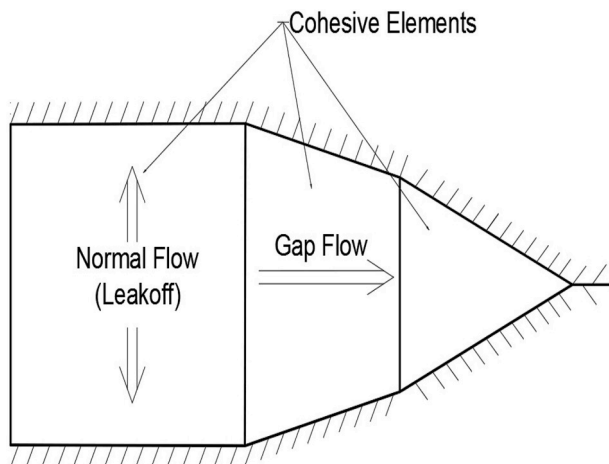


Fig. 2. Flow pattern of the fracturing fluid inside the cohesive element.

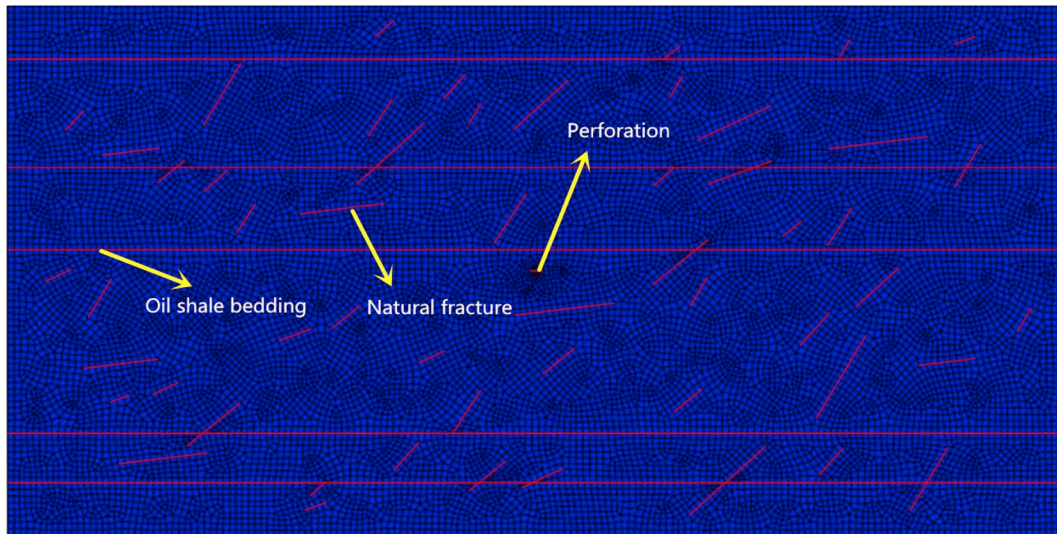


Fig. 3. Multiple media model of oil shale with the intersection angle setting as 90°. The red line (long) represents the bedding planes of the oil shale, the red line (short) represents the natural fractures and the short line in the middle of the model represents the perforation.

Table 1
Input parameters of the numerical simulation.

	Variables	Values
Rock Properties	Young's modulus (GPa)	8.4
	Poisson's ratio (–)	0.23
	Permeability coefficient (m/s)	1.7×10^{-12}
	Pore pressure (MPa)	2
Cohesive Zone Properties	Void ratio (–)	0.05
	Young's modulus (GPa)	8.4
	Normal nominal stress t_n (MPa)	1.81
	Nominal Stress (first direction) t_s (MPa)	5.18
	Nominal Stress (second direction) t_t (MPa)	5.18
	Damage evolution	0.0003
	Type: displacement (m)	
In situ Stress	Vertical stress, σ_v (MPa)	–4.4
	Maximal horizontal stress, σ_H (MPa)	–4.0
	Minimal horizontal stress, σ_h (MPa)	–3.85
	Viscosity of fracturing fluid (Pa·s)	0.001
Fluid Properties	Specific weight of the wetting liquid	9800

3. Results and discussion

The effects of the fracturing parameters, such as flow rate and viscosity of the fracturing fluid and length and direction of the perforation, are usually considered in the theoretical analyses, numerical simulations, and experimental measurements of hydraulic fracturing. Weak planes were embedded in the model by using a random function to simulate the random distributions of the weak planes in reservoirs. It was reported in the literature that the effects of viscosity and flow rate of the fracturing fluid on the hydraulic fracture propagation were similar (Guo et al., 2015c). Therefore, three fracturing parameters, including the flow rate of fracturing fluid, perforation length and the intersection angle between the direction of perforation and maximum *in-situ* stress, were investigated using the following orthogonal test.

3.1. Analysis of the orthogonal experiment results

In recent years, many scholars have used orthogonal tests and the significance test to analyse the effects of various parameters on the test indicators (Chen et al., 2019; Yang et al., 2018). Based on the three factors mentioned above, orthogonal test was designed to study the

effects of different fracturing parameters on the RRE. Table 2 presents the factors and levels used in the orthogonal test. The cumulative length and maximum width of the fractures were used as the evaluation indices of the RRE and analysed by the Analysis of variance (ANOVA) method. The results of the orthogonal experiment are shown in Table 3.

3.1.1. Variance analysis of the cumulative length of the hydraulic fracture

- (1) Calculation of the sum of the squared deviations of various factors.

Table 4 shows the sum of the squared deviations of various factors on the cumulative fracture length. The parameter K_{ij} is the sum of the test values corresponding to level i of factor j ; R_i and S_j represent the range and sum of the squared deviations, respectively; and T is the sum of the evaluation indices. The following is an example of a calculation process.

In the third column (factor B), the simulation results of test number 1, 6 and 8 correspond to the first level. Thus, $K_{12} = 22.41 + 32.32 + 35.67 = 90.40$. Likewise, the remaining K_{ij} can also be obtained.

- (2) Significance test based on ANOVA table: Cumulative length of the hydraulic fractures

The sum of the squares of the deviations can be obtained using the following equations:

$$S_j = \frac{1}{r} \left(K_{1j}^2 + K_{2j}^2 + K_{3j}^2 \right) - \frac{1}{n} T^2 \quad (7)$$

$$r = \frac{n}{m}$$

where n is the total number of tests and m is the number of levels. In this orthogonal test, n and m are 9 and 3, respectively.

Table 2
Factors and levels of the orthogonal experimental design.

Levels	Factors		
	(A) Flow rate (m ³ /s)	(B) Perforation length (m)	(C) Intersection angle (°)
1	0.001	0.4	0°
2	0.002	0.6	45°
3	0.003	0.8	90°

Table 3

Results of the orthogonal experiment.

Test Number	Factors				Evaluation indices	
	A	Error	B	C	Cumulative length of fracture, (m)	Maximum fracture width, (mm)
1	1	1	1	1	22.41	3.9
2	1	2	2	2	23.85	3.7
3	1	3	3	3	20.23	4.1
4	2	1	2	3	35.20	4.4
5	2	2	3	1	48.06	4.5
6	2	3	1	2	32.32	4.3
7	3	1	3	2	38.72	4.7
8	3	2	1	3	35.67	5.2
9	3	3	2	1	53.83	4.5

A, B and C represent the flow rate, perforation length and intersection angle, respectively.

Table 4

Sums of squared deviations.

(2) Significance test based on ANOVA table: Cumulative length of the hydraulic fractures

Parameters	Factors				T
	A	e	B	C	
K _{1j}	66.49	96.33	90.4	124.3	310.29
K _{2j}	115.58	107.58	112.88	94.89	
K _{3j}	128.22	106.38	107.01	91.1	
K _{1j} ²	4420.92	9279.47	8172.16	15450.49	
K _{2j} ²	13358.74	11573.46	12741.89	9004.11	
K _{3j} ²	16440.37	11316.7	11451.14	8299.21	
R _i	20.58	3.75	7.49	11.07	
S _j	708.92	25.45	90.64	220.18	

A, B, C and e represent the flow rate, perforation length, intersection angle, and error sequence, respectively.

Therefore, based on Equation (7), S_j can be obtained. For example:

$$S_A = \frac{1}{3} (4420.92 + 13358.74 + 16440.37) - \frac{1}{9} \times 310.29^2 = 708.92 \quad (8)$$

The sums of squared deviations of other factors can be obtained in the same way.

The degrees of freedom of the factors must be determined before calculating the squared sum of the average deviations. Without considering the interactions among various factors, the degrees of freedom were calculated according to the following equations:

$$f_A = f_B = f_C = f_e m - 1 \quad (9)$$

$$f_T = n - 1$$

The definitions of m and n are the same as those defined above. The corresponding results are displayed in the second column of Table 5. Based on the ratio of the sum of the squared deviations and the degrees of freedom, the squared sum of the average deviations can be calculated. The results are shown in the third column of Table 5.

Before performing the significance test, the corresponding F value must be checked, which is defined as the ratio of the squared sum of the average deviations of each factors and the error sequence. Based on the table of F-distribution and degrees of freedom mentioned above, the critical values can be determined. The F and critical values are shown in the fourth and fifth columns of Table 5, respectively. As $F \geq F_{0.01}(f_A, f_e)$, it indicates that the change in this factor has the most significant effect on the corresponding evaluation index, which is marked as “***”. As $F_{0.01}(f_A, f_e) > F \geq F_{0.05}(f_A, f_e)$, it implies that the change in this factor has a significant effect on the evaluation index, which is marked as “**”. As $F_{0.10}(f_A, f_e) > F$, it indicates that the change in this factor level has no significant effect on the evaluation index, which is marked as “-”.

Based on the F value of the fourth column in the ANOVA table, the

Table 5

Results of ANOVA table.

Source of Variance	S	f	V	F	Critical Value	Significance
A	708.92	2	354.46	27.84	$F_{0.10}(2,2) = 9$	*
B	90.64	2	45.32	3.56	$F_{0.05}(2,2) = 19$	-
C	220.18	2	110.09	8.65	$F_{0.01}(2,2) = 99$	-
Error	25.45	2	12.73			
T	1045.16	8				

S, f and V represent the sums of the squares of deviation, degree of freedom, and sum of squared of mean deviation, respectively.

primary and secondary order of the factors can be determined as A, C and B. Therefore, it can be concluded that the flow rate of the fracturing fluid has a significant impact on the cumulative fracture length, followed by the intersection angle. The perforation length, which is set as 0.6 m directly, has the least significant effect on the evaluation index. To achieve the maximal length of the hydraulic fractures, the preferred condition would be $A_3C_1B_2$.

3.1.2. Variance analysis of the maximum width of hydraulic fracture

Since the calculation process is similar, the computational process is not discussed in detail in this section. Table 6 shows the ANOVA results.

Similarly, it can be determined that the flow rate of the fracturing fluid has a significant impact on the maximum fracture width, followed by the intersection angle, and perforation length has the least significant impacts on the evaluation index. Therefore, the optimisation of the perforation length was not carried out subsequently and was directly set as 0.6 m. The preferred parameters to obtain the maximum fracture width is $A_3C_1B_2$.

In this section, the effects of three factors (flow rate, intersection angle, and perforation length) on the evaluation indicators were studied and the fracturing parameters were optimised using the orthogonal test. The significance test showed that the change of flow rate had a significant impact on both the evaluation indicators. However, the length of perforation had the least significant effect, which could be determined according to the specific conditions during the actual fracturing operation. Many researchers opined that the length of the perforation had almost no effect on the geometry of the fractures compared to the effects of other perforating parameters (Jiang et al., 2012; Wang et al., 2013; Zhao et al., 2016). These observations were consistent with the results of the orthogonal test obtained from this study as well. Based on the combination of the optimised parameters obtained above and the given level of factors in the orthogonal experiment, the preliminary optimal fracturing parameter was $A_3C_1B_2$, and the corresponding flow rate, intersection angle and perforation length values were 0.003 m³/s, 0° and 0.6 m, respectively.

Table 6

ANOVA results table.

Source of Variance	S	f	V	F	R _i	Critical Value	Significance
A	1.22	2	0.61	24.4	0.9	$F_{0.10}(2,2) = 9$	*
B	0.12	2	0.06	2.4	0.27	$F_{0.05}(2,2) = 19$	-
C	0.19	2	0.095	3.8	0.33	$F_{0.01}(2,2) = 99$	-
Error	0.05	2	0.025		0.17		
T	1.58	8					

S, f, V and R_i represent the sums of squares of deviation, degree of freedom, sum of the squared of mean deviation and range, respectively.

3.2. Effect of the flow rate of the fracturing fluid and intersection angle on the reservoir reconstruction efficiency (RRE)

Because the range of the levels of the factors level in the orthogonal test was limited, the optimal fracturing parameters obtained above could be treated as preliminary optimised parameters. Therefore, we conducted a single factor analysis to further explore the impact of the first two factors on the RRE and finally determined the optimal fracturing parameters for the oil shale reservoir. To avoid the influences of different distributions of weak planes on the results, we strictly controlled the location of the weak planes during the establishment of the model. The flow rate ranged from $0.0005 \text{ m}^3/\text{s}$ to $1 \text{ m}^3/\text{s}$ and the intersection angle was set to 0° , 45° , and 90° , respectively. The simulation results of some adjacent sets of variables were not much different; hence, only the representative results were selected for display in this section. Moreover, the orthogonal test determined that perforation length had almost no effect on the RRE, so we set it to 0.6 m in the model to simplify the process of investigations.

3.2.1. Investigations on the propagation process of hydraulic fracture

This section describes the studies carried out on the extension process and the morphology of hydraulic fractures in the model under different flow rates of the fracturing fluid. The letters A, B, or C indicates the initial intersection angle (the angle between the direction of perforation and the maximum principal stress) of 0° , 45° , 90° , respectively. The number after each letter (i.e., 1, 2, or 3) represents the entire morphology of the fractures after 10s, 60s, or 120s, respectively.

(a) Flow rate: $0.0005 \text{ m}^3/\text{s}$

As shown in Fig. 4-A1, the angle between the directions of the perforation and the maximum *in-situ* stress was 0° , i.e., the intersection angle was 0° . With increasing bottom-hole pressure, the hydro-fractures were initiated and expanded along the direction of the maximum

principal stress. The bedding plane and natural fracture A were crossed directly. Subsequently, the hydraulic fractures were deflected into the natural fracture under the induction of natural fracture B. This result confirmed that the fractures generally extended along the weak planes under a low flow rate (Chen et al., 2016; Guo et al., 2014). When the hydraulic fracture intersected with the natural fracture, the fracturing fluid swarmed into the natural fracture and caused the fluid pressure in the fracture to increase gradually. Until the fluid pressure in the fracture exceeded the normal effective stress on the natural fracture, the natural fracture was partially opened up, as shown in Fig. 4-A2. The propagation morphology of the hydraulic fracture was asymmetric. Compared with the upper wing of the hydraulic fracture, the lower wing extended rapidly and preferentially contacted the natural fracture. At the end of the fracturing process, the hydraulic fracture was partially closed because of the leakage of the stimulated natural fracture B as shown in Fig. 4-A3.

As the intersection angle was changed to 45° , the hydraulic fracture first extended along the direction of the perforation and then rapidly turned to the direction of the maximum principal stress, as shown in Fig. 4-B1. Similar to the intersection angle of 0° , the propagation morphology was also asymmetric. Fig. 4-B3 showed that the hydraulic fractures finally penetrated the tip of natural fracture B at the end of the process.

Based on the gradual increase of the intersection angle to 90° , while maintaining the flow rate, the hydraulic fracture propagated in the bedding plane direction and contacted natural fracture G. Based on the stimulation of the hydraulic fracture, the random distributions of both natural fracture G and bedding plane I were activated, as shown in Fig. 4-C1–C2. Because the permeability of the weak planes was far greater than that of the rock matrix, a large amount of fracturing fluid was lost and the hydraulic fracture was closed, as could be seen in Fig. 4-C3.

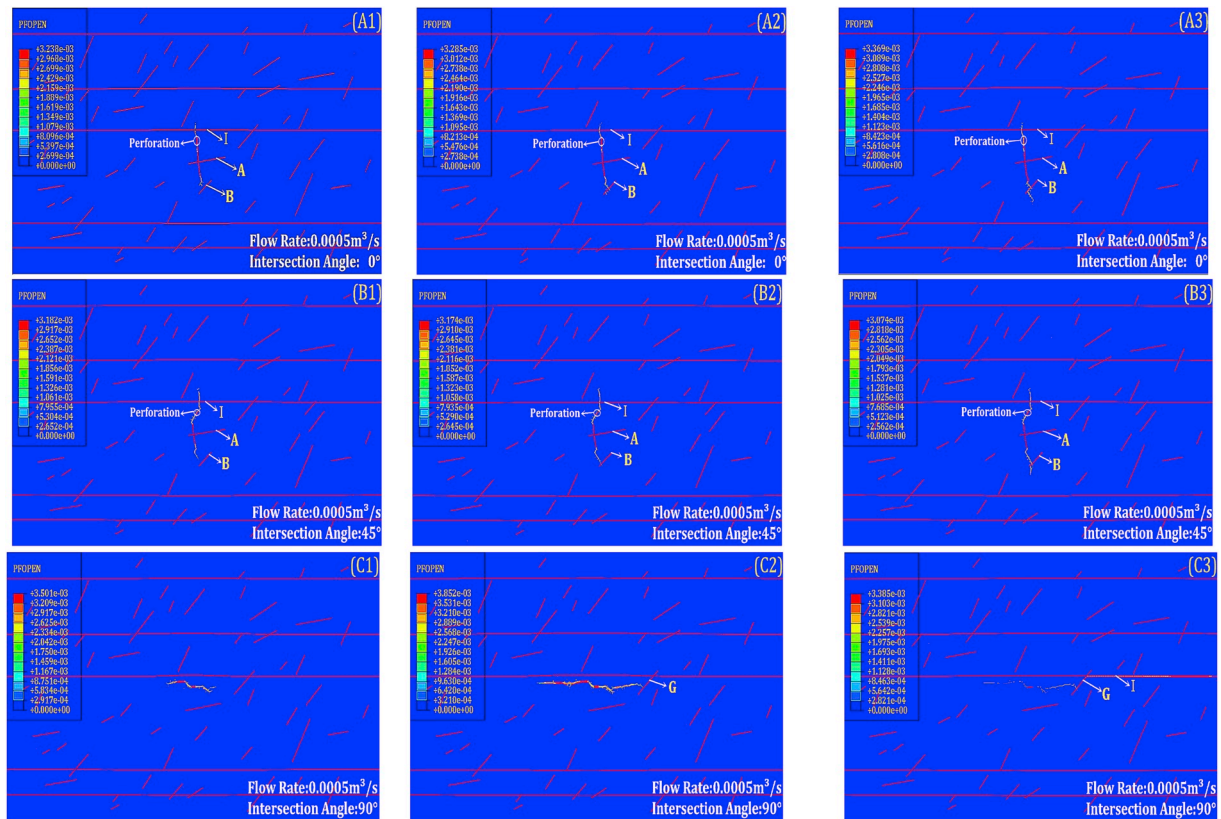


Fig. 4. Fracture extension processes with a flow rate of $0.0005 \text{ m}^3/\text{s}$ for different intersection angles: (A) 0° , (B) 45° and (C) 90° . The number after each letter represents the overall shape of the fractures corresponding to (1) 10 s, (2) 60 s, and (3) 120 s (total simulation time: 120 s).

The propagation morphology of the hydraulic fracture with a flow rate of $0.0005 \text{ m}^3/\text{s}$ was studied for three different types of intersection angles. The results showed that the natural fractures would cause the hydraulic fractures to deviate from the direction of the maximum principal stress. Under this flow rate, the leakage of the rock matrix and the weak planes limited the extension of the hydraulic fractures and no branch fractures were generated in the model. As shown by the leftmost point in Figs. 8 and 9, the cumulative fracture length and maximum fracture width were both very small, which implied that the RRE was also quite low for this flow rate. Under the minimal flow rate conditions, the leakage of the weak planes had a great influence on the fracture morphology. The side of the hydraulic fracture that first contacted the natural fracture would expand rapidly and the whole hydraulic fracture showed an asymmetrically extended pattern. As the intersection angle increased, the hydraulic fracture first extended in the direction of the perforation and then gradually bent towards the direction of the maximum principal stress. The greater the intersection angle, the larger the degree of bending.

(b) Flow rate: $0.005 \text{ m}^3/\text{s}$

The asymmetric propagation morphology of the hydraulic fractures gradually disappeared with an increased flow rate, as shown in Fig. 5. At the same time, the length and width of the fractures significantly increased.

As the flow rate increased by a factor of ten, branch fractures **a** and **b** were formed when the hydraulic fracture intersected with natural fracture B, as illustrated in Fig. 5-A1. With the continuous pumping of the fracturing fluid, branch fracture **b** rapidly propagated under the induction of natural fracture E and became a main fracture, as shown in Fig. 5-A2. However, branch fracture **a** was forced to close because natural fractures D and E were activated, as illustrated in Fig. 5-A3.

When the intersection angle was changed to 45° , the hydraulic fracture was deflected into the direction of maximum principal stress

and two branch fractures **a** and **d** simultaneously extended, as shown in Fig. 5-B1. Fig. 5-B2 showed that branch fracture **a** propagated horizontally and intersected with natural fracture G, and branch fractures **b** and **c** were generated after the intersection of the hydraulic fracture and natural fracture B. At the end of the process, branch fractures **b** and **c** rapidly propagated under the induction of natural fractures E and F and the branch fractures were closed due to the stimulation of natural fracture G, as shown in Fig. 5-B3.

It could be seen from Fig. 5-C1–C2, natural fracture G was activated by the hydraulic fractures extending horizontally and bedding plane I was partially opened by the stimulated natural fracture G. As shown in Fig. 5-C3, the activation of bedding plane I promoted the rapid growth of the right wing of the hydraulic fracture. However, the left-wing propagation of the hydraulic fracture was limited owing to the leakage of a large amount of fracturing fluid along the bedding plane.

In this section, the extension behaviour of the hydraulic fractures under this flow rate of $0.005 \text{ m}^3/\text{s}$ was observed. The results showed that the increase in flow rate (by a factor of ten) advanced the length and width of the fracture extension and the morphology of asymmetric extension gradually disappeared. In addition, the branch fractures began to appear under this flow rate. It could be seen from Figs. 8 and 9, compared to the flow rate of $0.0005 \text{ m}^3/\text{s}$, in this case the extension of hydraulic fractures and the initiation of branch fractures resulted in a significant improvement of the cumulative fracture length and the maximum fracture width, which implied that the increase in the flow rate would promote an obvious rise in the RRE. However, this flow rate ($0.005 \text{ m}^3/\text{s}$) could not maintain the extension of the branch fractures for the simulated formation.

(c) Flow rate: $0.01 \text{ m}^3/\text{s}$

Fig. 6-A3 showed that the branch fractures **c** and **d** were generated induced by natural fracture E and F. Similar to the case of the earlier flow rate, the width of branch fracture **a** reduced under the activation of

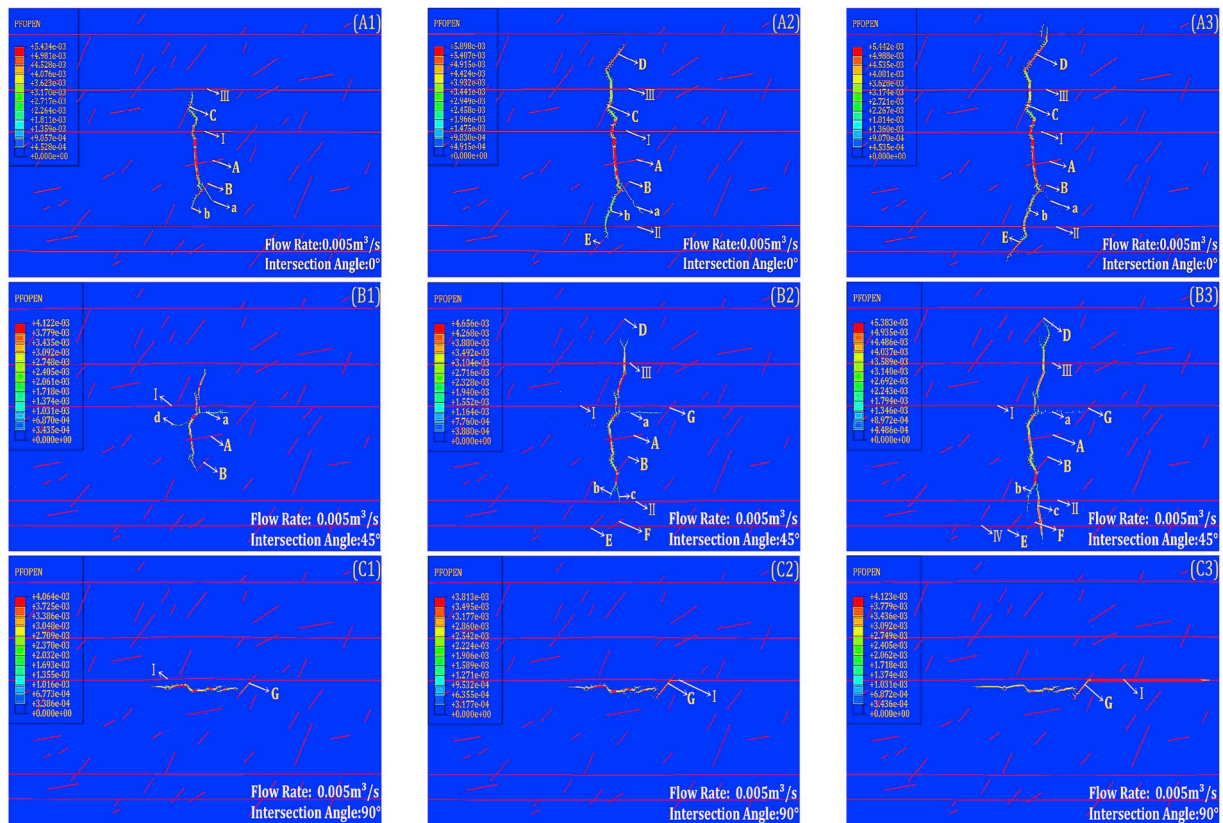


Fig. 5. Fracture extension processes with a flow rate of $0.005 \text{ m}^3/\text{s}$ for different intersection angles: (A) 0° , (B) 45° and (C) 90° . The number after each letter represents the overall shape of the fractures corresponding to (1) 10 s, (2) 60 s and (3) 120 s. (total simulation time: 120 s)

natural fractures E and F, but the fracture was not completely closed.

Compared with the flow rate of $0.005 \text{ m}^3/\text{s}$, branch fractures **a** and **b** continued to extend after natural fracture G was activated as the angle was changed to 45° , as shown in Fig. 6-B2. Subsequently, the branch fracture passed through the end of natural fracture G and gradually turned to the direction of maximum principal stress. Induced by natural fracture D, branch fracture **c** extended rapidly, as illustrated in Fig. 6-B3.

Fig. 6-C1 showed that branch fracture **a** was generated and extended in the direction of the maximum principal stress under the action of the fracturing fluid when the perforation was perpendicular to the direction of the maximum principal stress. At the same intersection angle, compared with the previous flow rate, the bending degree of the left-wing increased and gradually turned to the direction of maximum principal stress. At the end of the process, branch fracture **a** and the right-wing of the hydraulic fracture rapidly extended under the influence of natural fractures D and H, as shown in Fig. 6-C3.

In this section, we studied the fracture propagation pattern at different intersection angles at a flow rate of $0.01 \text{ m}^3/\text{s}$. The simulation results showed that extension of the branch fractures could be maintained by increasing the flow rate after communicating with natural fractures. The bending degree of the fractures also increased, especially when the intersection angle was 90° . Therefore, as the flow rate was increased and the intersection angle was decreased, the full extension of the hydraulic fractures could be achieved and the RRE could be improved. These findings are consistent with the observations made by earlier studies that a high flow rate would promote the formation and extension of main hydraulic fractures (Cheng et al., 2015a; Yushi et al., 2015) and that the width of fractures and the generation of branch fractures would be increased and promoted (Guo et al., 2015d).

The number of stimulated natural fractures and the generated branch fractures during the hydraulic fracture propagation had a significant effect on the RRE. Based on the numerical simulation results, the

number of fractures of both the above types generated in this model are summarised in Table 7.

Based on the analysis of the data in Table 7, it could be concluded that the hydraulic fractures stimulated more natural fractures and promoted more branch fractures as the flow rate was increased and the intersection angle was decreased.

(d) Flow rate: $1 \text{ m}^3/\text{s}$

The fracture propagation behaviour after increasing the flow rate to an extremely high value of $1 \text{ m}^3/\text{s}$ is shown in Fig. 7. The continuous pumping of the fracturing fluid at this flow rate caused the bottom-hole pressure to rise instantaneously. This in turn, promoted multiple points of the matrix rock around the perforation to reach the initiation pressure and led to the formation of high-density radial branch fractures. Because the spacing of the branch fractures was very small, there was strong interference among the fractures. This had a restraining effect on the extension of the branch fractures and the formation of the main hydraulic fracture. Ultimately, only the vicinity of the wellbore was stimulated and the RRE of the whole model was extremely low.

Table 7

Numbers of branch and stimulated natural fractures.

Flow rate	Intersection angle	Number of branch fractures	Number of stimulated natural fractures
0.0005 (m^3/s)	0°	0	2
	45°	0	2
	90°	0	1
0.005 (m^3/s)	0°	2	5
	45°	2	3
	90°	0	1
0.01 (m^3/s)	0°	3	6
	45°	3	5
	90°	2	4

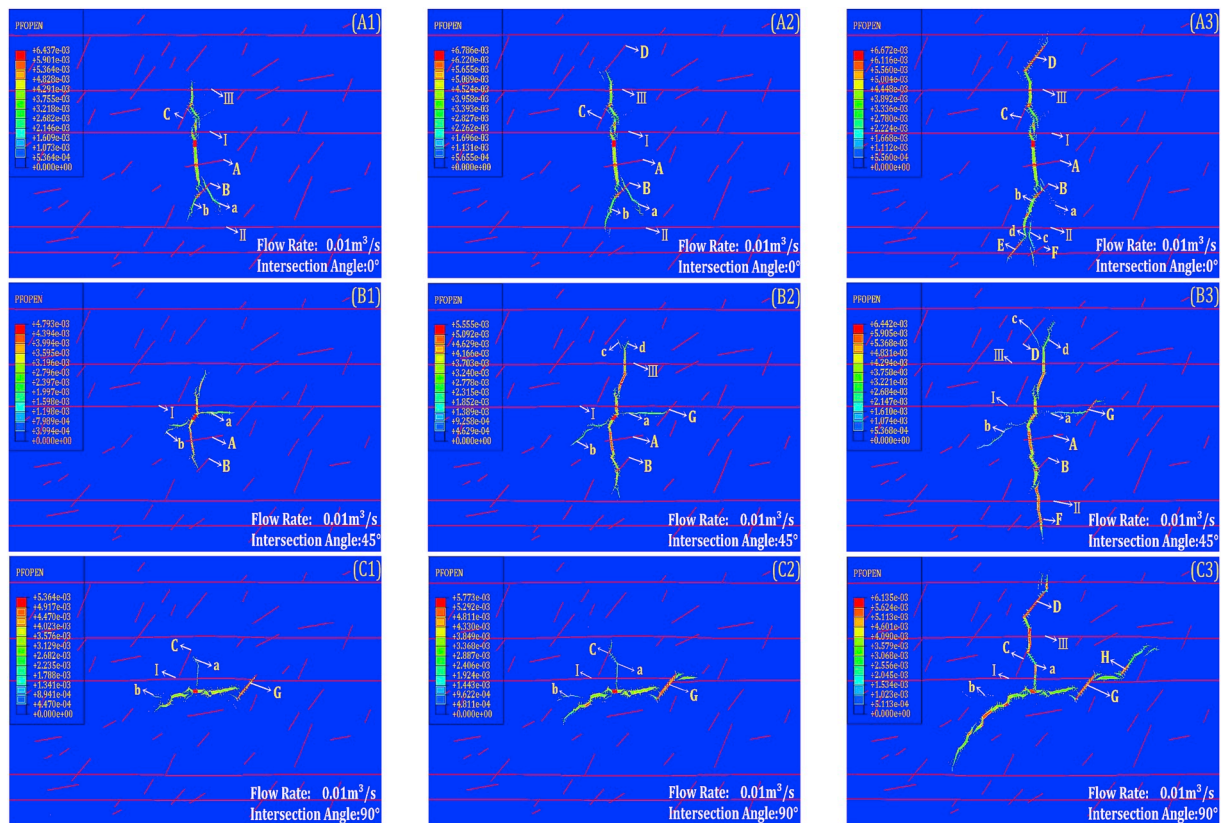


Fig. 6. Fracture extension processes with a flow rate of $0.01 \text{ m}^3/\text{s}$ for different intersection angles: (A) 0° , (B) 45° and (C) 90° . The number after each letter represents the overall shape of fractures corresponding to (1) 10 s, (2) 60 s and (3) 120 s. (total simulation time: 120 s)

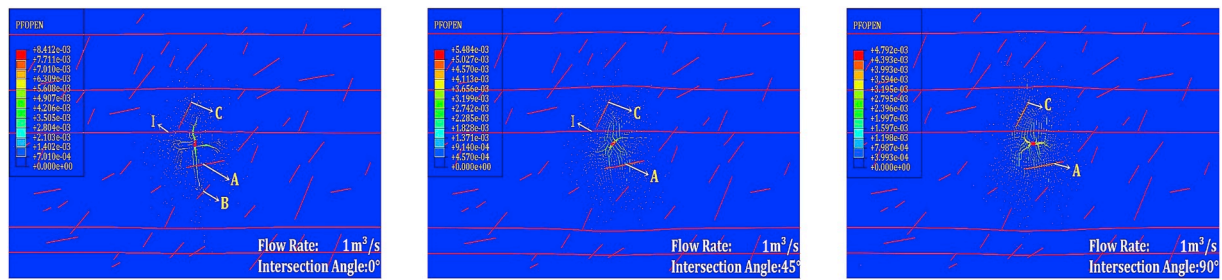


Fig. 7. Fracture extension processes with a flow rate of $1 \text{ m}^3/\text{s}$ for different intersection angles: 0° , 45° and 90° . (total simulation time: 120 s)

When reservoir reconstruction was carried out at a low flow rate, as shown in Fig. 4, the leakage of the rock matrix and the weak planes had a significant influence on the RRE, which caused the slow increase in the fluid pressure in the fracture and hindered the propagation of the hydraulic fracture. Compared to the rock matrix, the weak planes had a higher permeability and lower tensile and shear strengths; therefore, the weak planes could be activated at a low fluid pressure and extended as parts of the hydraulic fractures. Furthermore, when the flow rate of the fracturing fluid was low, the extension of the main hydraulic fracture was extremely difficult or even stopped in the matrix and the hydraulic fracture tended to extend along the weak planes that randomly developed in the reservoir. The hydraulic fractures on the side that preferentially contacted the weak planes that were randomly distributed in the model extended rapidly. It was considered that fracturing at very low flow rate should be avoided to the extent possible, as it would lead to an asymmetric extension pattern and limit the extension of hydraulic fractures. Under the dual leakage of the rock matrix and the natural fractures, the RRE (the cumulative fracture length and the maximum fracture width) was also be restricted and could not fully stimulate the reservoir.

With the increasing flow rate, the effect of the leakage gradually was weakened owing to the timely replenishment of the fracturing fluid from the main fracture. The net pressure of the fluid in the fracture also increased. Consequently, the hydraulic fractures extended in the rock matrix and the asymmetric extension behaviour, mentioned above, gradually disappeared. In general, the more the natural fractures were distributed in the reservoir, the greater the flow rate needed to promote the extension of the hydraulic fractures. As the fluid pressure in the fractures exceeded the fracture pressure at a certain point in the oil shale, the branch fractures were formed. The promotion of the formation and extension of the branch fractures significantly improved the RRE. Based on the simulation results, the flow rate for branch fracture initiation was $0.005 \text{ m}^3/\text{s}$. However, the extension of branch fracture could not be maintained at this flow rate. Once the natural fracture was activated, the fluid pressure inside the main and the branch fractures decreased instantaneously because the fracturing fluid flowed into the natural fractures and led to the closure of the branch fractures. When the flow rate was further increased to $0.01 \text{ m}^3/\text{s}$, the lost fracturing fluid would be replenished from the main fracture and the extension of the branch fracture could be maintained. Owing to the continuous extension of the hydraulic fractures and the branch fractures in the model, the cumulative fracture length and the maximum fracture width reached a fairly high level, which meant that a better RRE was achieved. In addition, the simulation results showed that the induction of the natural fractures also promoted the generation of branch fractures, as shown in Fig. 5-B3 and Fig. 6-B3. However, the mechanism controlling the introduction of branch fractures by the natural fractures needs to be further explored. When the flow rate of the fracturing fluid was increased to an extremely high level, for example, $1 \text{ m}^3/\text{s}$ in this study, multiple points around the perforation simultaneously reached the initiation state, which led to the generation of a large number of branch fractures. We considered that the main hydraulic fractures were formed by the merging of tiny branch fractures near the perforation. Therefore,

the formation of the main fractures was limited by the strong stress interference among the branch fractures. Under this flow rate of $1 \text{ m}^3/\text{s}$, only the reservoir near the perforation was vigorously stimulated and no main hydraulic fractures extended into the reservoir. Hence, this resulted in great waste of energy and an extremely low RRE.

In summary, the key to the formation of a complex fracture network is the optimisation of the flow rate of the fracturing fluid and direction of the perforation. To improve the RRE, an appropriate fracturing fluid flow rate and intersection angle must be selected according to the properties of reservoir rock matrix and the weak plane distribution before the fracturing. This will ensure a full utilisation of the random occurrences of the natural fractures in the reservoir and promote the generation of branch fractures and the extension of hydraulic fractures.

3.2.2. Contrast analysis of the RRE under different fracturing fluid flow rates and intersection angles

Here, the cumulative fracture length and the maximum fracture width were as the evaluation indices to measure the RRE. After the simulation results were processed using the Python scripts, the evaluation index values for different flow rates were obtained.

Based on Fig. 8, it could be observed that the cumulative length of the fractures at different intersection angles increased with as the flow rate increased. When the flow rate was below $0.001 \text{ m}^3/\text{s}$, the leakage of the weak surface and the matrix in the reservoir made it difficult to hold the fluid pressure in the fractures; therefore, the propagation of hydraulic fractures was inhibited. We found that no hydraulic fractures were generated when the flow rate was below $0.0005 \text{ m}^3/\text{s}$, which was the minimum flow rate required to generate the hydraulic fractures for the simulated reservoir. As the flow rate gradually increased, the fluid pressure in the fracture promoted the extension of the hydraulic fracture and activated the weak planes. The bedding planes then became part of the hydraulic fracture, as shown in Fig. 4-C3. As the flow rate of the fracturing fluid was increased to about $0.005 \text{ m}^3/\text{s}$, the bedding plane was disturbed and rapidly stimulated, which resulted in the generation of the largest cumulative fracture length, when the direction of the perforation was perpendicular to the direction of the maximum principal stress. If the flow rate continued to be increased at the same intersection angle, it was impossible to form effective hydraulic fractures in the reservoir matrix. This is because a large amount of fracturing fluid would leak along the activated bedding plane, which would result in the slow growth of the cumulative length of the fractures. As for the other two intersection angles, the increase in the flow rate promoted the extension of hydraulic fractures in the rock matrix, which promoted the communication with more natural fractures that were distributed in reservoir, and generated multiple branch fractures around the hydraulic fracture. This in turn, led to an increase in the cumulative fracture length. Moreover, it was confirmed that the greater the intersection angle, the larger the bending degree of the hydraulic fracture. This finding was consistent with the observation made by numerous earlier studies that the misorientation of the perforations caused the tortuous morphology of the near-wellbore fractures (Fallahzadeh et al., 2014; Guangqing and Mian, 2009; Hossain et al., 2000; Lei et al., 2015; Xie et al., 2018a). Therefore, the corresponding friction along the fractures

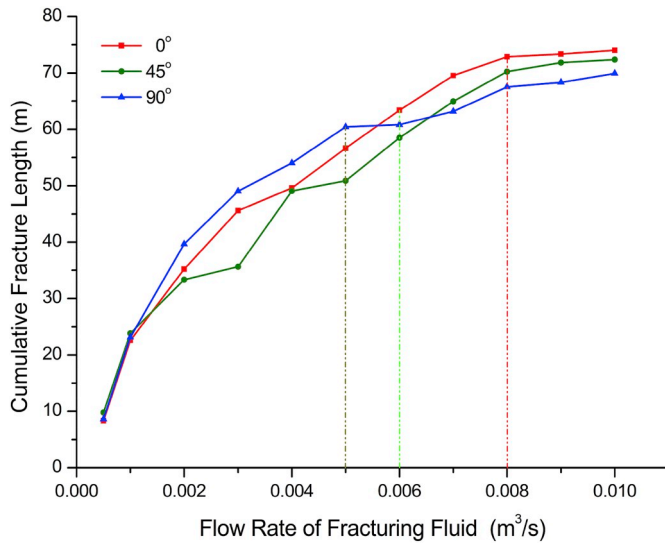


Fig. 8. Cumulative fracture length for various flow rates and intersection angles. (total simulation time: 120 s)

gradually increased and led to the decrease of the cumulative fracture length with a rise of the intersection angle.

Fig. 8 shows an interesting and crucial flow rate value. Although the cumulative length of the hydraulic fracture increased with increasing fracturing fluid flow rate, the simulated reservoir had a critical value of $0.008 \text{ m}^3/\text{s}$. When the flow rate reached this critical value, the growth rate of the cumulative fracture length tended to be stable at three different intersection angles. The influence of the increasing flow rate on the increase in the cumulative fracture length was gradually weakened. The existence of this critical flow rate indicates that blindly increasing the flow rate of the fracturing fluid would be futile with respect to improving the RRE.

Similarly, the coordinates of the cohesive elements could be handled by using the python language and the maximum fracture width of the hydraulic fractures at each flow rate could be obtained.

Fig. 9 shows the maximum fracture width at intersection angles of 0° , 45° , and 90° under different flow rates of the fracturing fluid. The simulation results showed that the hydraulic fracture mainly extended in the bedding plane of the simulated formation and the closure pressure

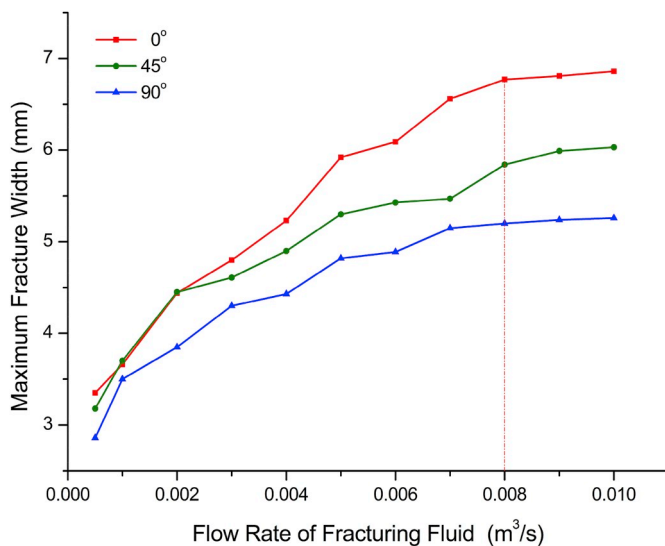


Fig. 9. Maximum fracture width for various flow rates and intersection angles. (total simulation time: 120 s)

of the fracture was approximately equal to the maximum principal stress of the formation, when the direction of the perforation was vertical to the direction of the maximum principal stress. In other words, the intersection angle equals to 90° . Therefore, the fracture width generated at this intersection angle was the smallest. In contrast, if the intersection angle was 0° , the principal part of the fracture extended along the direction of the maximum principal stress and the closure-pressure was approximately equal to the minimum horizontal principal stress. Consequently, the maximum fracture width would be obtained at the same flow rate when the perforation was parallel to the direction of maximum principal stress. As mentioned above, the diversion of the main fracture during the fracture propagation would increase the energy dissipation of the fluid in the fracture. When the intersection angle was 45° , the bending degree of the fracture was greater than that at 0° and the closure pressure was less than at the intersection angle of 90° . Therefore, the maximum fracture width obtained under different perforation directions was in the order of 0° , 45° , and 90° .

The graph showed that the maximum fracture width of the hydraulic fracture at three intersection angles increased with increasing flow rate. Similar to the description above, there was a critical value ($0.008 \text{ m}^3/\text{s}$) for the effect of flow rate on the increase in the maximum fracture width. The growth rate of the maximum fracture width decreased when the flow rate increased beyond this critical value. Therefore, it would be of no benefit to use a high-flow injection rate without any limit in the fracturing operation to achieve a larger fracture width.

In addition, the significance test showed that the perforation length had almost no effect on the RRE. Therefore, the length of the perforation was not optimised and kept constant at 0.6 m in this study. Furthermore, for the simulated reservoir, we found that continuing to increase the flow rate would be futile for increasing the RRE (cumulative fracture length and maximum fracture width) after the flow rate reached $0.008 \text{ m}^3/\text{s}$. With respect to the strata simulated in this study, the optimum RRE could be obtained when the flow rate was $0.008 \text{ m}^3/\text{s}$. The direction of the perforation should be as close to the direction of the maximum principal stress as possible.

As the hydraulic fracturing is a complex multi-physics coupling process, it should be understood that the method proposed in this study still has two main limitations. The first is the limitation of the element. To simulate the fluid-solid coupling process of hydraulic fracture, for the matrix element of oil shale only the quadrilateral element with pore pressure and displacement, i.e. CPE4P can be chosen. This type of element can be used to simulate the deformation of the rock matrix and the seepage of the fracturing fluid from the fractures to the rock matrix. However, being restricted to only quadrilateral elements can render the process of mesh quality optimisation difficult. Thus, some mesh shapes that in the model are not conducive to the calculations. The second limitation is the computational efficiency. Compared to the linear elastic fracture mechanics (LEFM), the computational efficiency of CZM is lower owing to the complexity of the selected traction-separation law. The average calculation time for a single computational model covered in this article is quite large.

4. Conclusions

The reservoir reconstruction efficiency (RRE) of Wangqing oil shale was analysed in this study based on the CZM. The notable differences from previous research are the use of random function to set up the weak planes with random distribution state in the model, and the introduction of zero-thickness cohesive elements at all boundaries of the meshes instead of pre-defined propagation paths of the fractures. Based on the model established above, the following conclusions can be drawn:

- (1) The results of the orthogonal test demonstrate that the flow rate of the fracturing fluid is the most significant factor affecting the RRE, followed by the intersection angle. The length of the perforation has almost no effect. For the rock and reservoir

conditions assumed in this study and the given levels in the orthogonal test, the preliminary optimisation of the fracturing parameters is $A_3C_1B_2$ and the corresponding flow rate, intersection angle and perforation length are $0.003 \text{ m}^3/\text{s}$, 0° and 0.6 m , respectively.

- (2) The investigation of the propagation behaviour of hydraulic fractures under the effects of the flow rate and intersection angle yields the following observations: (a) When the flow rate is low ($0.0005 \text{ m}^3/\text{s}$), the leakage of the rock matrix and weak surface has a great influence on the fracture extension. The fracture presents an asymmetric morphology and the side that preferentially contacts the natural fractures extends rapidly. (b) With increasing flow rate, the asymmetric morphology mentioned above gradually disappears and the RRE increases as well. When the flow rate is $0.005 \text{ m}^3/\text{s}$, the branch fractures begin to appear; however, this flow rate cannot maintain the extension of the branch fractures when the weak planes are stimulated by the fractures. (c) As the flow rate changes to $0.01 \text{ m}^3/\text{s}$, both the main and branch fractures are fully extended and the activation of weak planes does not lead to the closure of the branch fractures at this flow rate. Therefore, the higher the density of the weak surface system in the reservoir, the higher the flow rate required to maintain the extension of the hydraulic and branch fractures. (d) When the flow rate is increased to obtain a higher cumulative fracture length and maximum fracture width, high-density radial fractures are generated near the perforation at the flow rate of $1 \text{ m}^3/\text{s}$ and the extension of the main fractures is limited by the stress interference between the fractures, which is unfavourable for the exploration of the reservoir. Hence, the distribution of weak planes should be carefully considered when choosing the fracturing flow rate of the reservoir. With respect to the intersection angle, the smaller the angle (i.e., the direction of the perforation is approximately parallel to the direction of the maximum principal stress) the larger the length and width of the fractures and thus, more natural fractures are stimulated.
- (3) An interesting and crucial point based on the single factor analysis of the flow rate is that the growth rate of the RRE decreases or even stagnates when the flow rate increases to a critical value of $0.008 \text{ m}^3/\text{s}$, which represents the optimal flow rate required to stimulate the simulated reservoir. Therefore, it can be inferred that it is blindly increasing the flow rate to a high level without restricting the actual fracturing operation will not improve the RRE. Combined with the aforementioned orthogonal test results, it can be concluded that the optimal fracturing parameters for the rock and reservoir conditions assumed in this paper are as follows: a flow rate $0.008 \text{ m}^3/\text{s}$ of the fracturing fluid and an intersection angle of 0° between the direction of the perforation and maximum *in-situ* stress.

These results contribute to the prediction of the morphology of hydraulic fracture propagation in oil shale reservoirs before the fracturing operation and provide optimal fracturing parameters for the target reservoir. This is of great significance for the future *in-situ* development of oil shale resources in the Wangqing area.

Author contributions section

Lianghao Zhai: Lianghao Zhai has made substantial contributions in writing papers, designing ideas, collecting data **Han Zhang:** Han Zhang made key revisions to the academic content of this article. **Dongbin Pan and Ying Zhu:** Dongbin Pan analysed the results of the simulation and Ying Zhu verified the corresponding results. **Jiang Zhu and Ying Zhang:** They translated the full text. **Chen Chen*:** Chen Chen considered that cohesive zone method can be used to simulate the propagation of hydraulic fractures in oil shale reservoir.

Declaration of competing interest

We declare that we do not have any commercial or associative interest that represents a conflict of interest in connection with the work submitted. The manuscript entitled, "Optimisation of hydraulic fracturing parameters based on cohesive zone method in oil shale reservoir with random distribution of weak planes"

Acknowledgement

This work was supported by the National Natural Science Foundation of China (No. 41876218 and No. 41672361). Ministry of Land and Resources of the People's Republic of China (No. 201311041). Department of Science and Technology of Jilin Province (No. 20170414044 GH and No. 20160204011SF). Department of Science and Technology of Jilin Province (No. SXGJSF2017-5) and Jilin University (No.2017TD-24). The authors also express their appreciation to technical reviewers for their constructive comments.

References

- AbuAisha, M., Eaton, D., Priest, J., Wong, R., 2017. Hydro-mechanically coupled FDEM framework to investigate near wellbore hydraulic fracturing in homogeneous and fractured rock formations. *J. Pet. Sci. Eng.* 154, 100–113.
- Arias, I., Knap, J., Chalivendra, V.B., Hong, S., Ortiz, M., Rosakis, A.J., 2007. Numerical modelling and experimental validation of dynamic fracture events along weak planes. *Comput. Methods Appl. Mech. Eng.* 196 (37–40), 3833–3840.
- Belytschko, T., Black, T., 1999. Elastic crack growth in finite elements with minimal remeshing. *Int. J. Numer. Methods Eng.* 45, 601–620.
- Bing, H., Mian, C., Zhimeng, L., Yonghui, W., Ce, D., 2014. Propagation area evaluation of hydraulic fracture networks in shale gas reservoirs. *Pet. Explor. Dev.* 41, 833–838.
- Bryant, E.C., Hwang, J., M Sharma, M., 2015. Arbitrary Fracture Propagation in Heterogeneous Poroelastic Formations Using a Finite Volume-Based Cohesive Zone Model. *Society of Petroleum Engineers*.
- Carrier, B., Granet, S., 2012. Numerical modeling of hydraulic fracture problem in permeable medium using cohesive zone model. *Eng. Fract. Mech.* 79, 312–328.
- Chen, C., Pan, D., Yang, L., Zhang, H., Li, B., Jin, C., Li, X., Cheng, Y., Zhong, X., 2019. Investigation into the water jet erosion efficiency of hydrate-bearing sediments based on the arbitrary Lagrangian-eulerian method. *Appl. Sci.* 9 (1), 182.
- Chen, Z., Jeffrey, R.G., Zhang, X., Kear, J., 2016. Finite-element simulation of a hydraulic fracture interacting with a natural fracture. *SPE J.*
- Chen, Z., Bunger, A.P., Xi, Z., Jeffrey, R.G., 2009. Cohesive zone finite element-based modeling of hydraulic fractures. *Acta Mech. Solida Sin.* 22 (5).
- Cheng, W., Jin, Y., Chen, M., 2015a. Reactivation mechanism of natural fractures by hydraulic fracturing in naturally fractured shale reservoirs. *J. Nat. Gas Sci. Eng.* 23, 431–439.
- Cheng, W., Jin, Y., Lin, Q., Chen, M., Zhang, Y., Diao, C., Hou, B., 2015b. Experimental investigation about influence of pre-existing fracture on hydraulic fracture propagation under tri-axial stresses. *Geotech. Geol. Eng.* 33, 467–473.
- Choo, L.Q., Zhao, Z., Chen, H., Tian, Q., 2016. Hydraulic fracturing modeling using the discontinuous deformation analysis (DDA) method. *Comput. Geotech.* 76, 12–22.
- Chuprakov, D.A., Akulich, A.V., Siebrits, E., Thiercelin, M., 2011. Hydraulic-fracture propagation in a naturally fractured reservoir. *SPE Prod. Oper.* 26, 88–97.
- Dahi Taleghani, A., Gonzalez, M., Shojaei, A., 2016. Overview of numerical models for interactions between hydraulic fractures and natural fractures: challenges and limitations. *Comput. Geotech.* 71, 361–368.
- Dehghan, A.N., Goshtasbi, K., Ahangari, K., Jin, Y., 2015. Experimental investigation of hydraulic fracture propagation in fractured blocks. *Bull. Eng. Geol. Environ.* 74, 887–895.
- Fallahzadeh, S.H., Rasouli, V., Sarmadivaleh, M., 2014. An investigation of hydraulic fracturing initiation and near-wellbore propagation from perforated boreholes in tight formations. *Rock Mech. Rock Eng.* 48 (2), 573–584.
- Fatahi, H., Hossain, M.M., Sarmadivaleh, M., 2017. Numerical and experimental investigation of the interaction of natural and propagated hydraulic fracture. *J. Nat. Gas Sci. Eng.* 37, 409–424.
- Gale, J.F.W., Laubach, S.E., Olson, J.E., Eichhubl, P., Fall, A., 2014. Natural fractures in shale: a review and new observations. *AAPG (Am. Assoc. Pet. Geol.) Bull.* 98, 2165–2216.
- Gale, J.F.W., Reed, R.M., Holder, J., 2007. Natural fractures in the Barnett Shale and their importance for hydraulic fracture treatments. *AAPG (Am. Assoc. Pet. Geol.) Bull.* 91, 603–622.
- Guangqing, Z., Mian, C., 2009. Complex fracture shapes in hydraulic fracturing with orientated perforations. *Pet. Explor. Dev.* 36 (1), 103–107.
- Guo, J., Lu, Q., Zhu, H., Wang, Y., Ma, L., 2015a. Perforating cluster space optimization method of horizontal well multi-stage fracturing in extremely thick unconventional gas reservoir. *J. Nat. Gas Sci. Eng.* 26, 1648–1662.
- Guo, J., Luo, B., Lu, C., Lai, J., Ren, J., 2017. Numerical investigation of hydraulic fracture propagation in a layered reservoir using the cohesive zone method. *Eng. Fract. Mech.* 186, 195–207.

- Guo, J., Zhao, X., Zhu, H., Zhang, X., Pan, R., 2015b. Numerical simulation of interaction of hydraulic fracture and natural fracture based on the cohesive zone finite element method. *J. Nat. Gas Sci. Eng.* 25, 180–188.
- Guo, T., Zhang, S., Gao, J., Zhang, J., Yu, H., 2013. Experimental study of fracture permeability for stimulated reservoir volume (SRV) in shale formation. *Transp. Porous Media* 98, 525–542.
- Guo, T., Zhang, S., Qu, Z., Zhou, T., Xiao, Y., Gao, J., 2014. Experimental study of hydraulic fracturing for shale by stimulated reservoir volume. *Fuel* 128, 373–380.
- Guo, T., Zhang, S., Zou, Y., Xiao, B., 2015c. Numerical simulation of hydraulic fracture propagation in shale gas reservoir. *J. Nat. Gas Sci. Eng.* 847–856.
- Guo, T., Zhang, S., Zou, Y., Xiao, B., 2015d. Numerical simulation of hydraulic fracture propagation in shale gas reservoir. *J. Nat. Gas Sci. Eng.* 26, 847–856.
- Hossain, M.M., Rahman, M.K., Rahman, S.S., 2000. Hydraulic fracture initiation and propagation: roles of wellbore trajectory, perforation and stress regimes. *J. Pet. Sci. Eng.* 27, 129–149, 2000.
- Jiang, M.Z., Li, Y., Zhang, Y.M., Jiang, T.X., Liu, M.X., 2012. Influence of perforation parameter on crack initiation and extending of hydraulic fracturing. *Adv. Mater. Res.* 594–597, 202–206.
- Jing, L., Ma, Y., Fang, Z., 2001. Modeling of fluid flow and solid deformation for fractured rocks with discontinuous deformation analysis (DDA) method. *Int. J. Rock Mech. Min. Sci.* 38, 343–355.
- Kang, Z., Yang, D., Zhao, Y., Hu, Y., 2011. Thermal cracking and corresponding permeability OF FUSHUN oil shale. *Oil Shale* 28 (2), 273–283.
- Lei, X., Zhang, S., Xu, G., Zou, Y., 2015. Impact of perforation on hydraulic fracture initiation and extension in tight natural gas reservoirs. *Energy Technol.* 3 (6), 618–624.
- Liang, Y., Cheng, Y., Zou, Q., Wang, W., Ma, Y., Li, Q., 2017. Response characteristics of coal subjected to hydraulic fracturing: an evaluation based on real-time monitoring of borehole strain and acoustic emission. *J. Nat. Gas Sci. Eng.* 38, 402–411.
- Nagel, N.B., Sanchez-Nagel, M.A., Zhang, F., Garcia, X., Lee, B., 2013. Coupled numerical evaluations of the geomechanical interactions between a hydraulic fracture stimulation and a natural fracture system in shale formations. *Rock Mech. Rock Eng.* 46, 581–609.
- OTS, A., 2005. Oil shale as a power fuel. *Oil Shale* 22, 367–368.
- Shi, F., Wang, X., Liu, C., Liu, H., Wu, H., 2016. A coupled extended finite element approach for modeling hydraulic fracturing in consideration of proppant. *J. Nat. Gas Sci. Eng.* 33, 885–897.
- Shuai, G., 2017. Study on Crack and Extension Mechanism of Oil Shale Hydraulic Fracturing in Horizontal Well. Dr. Thesis, Jilin university.
- Sun, K.M., Tan, J., Wu, D., 2012. The research on dynamic rules of crack extension during hydraulic fracturing for oil shale in-situ exploitation. In: 2011 International Conference of Environmental Science and Engineering, vol. 12, pp. 736–743. Pt B, 12.
- Taleghani, A.D., Gonzalez-Chavez, M., Yu, H., Asala, H., 2018. Numerical simulation of hydraulic fracture propagation in naturally fractured formations using the cohesive zone model. *J. Pet. Sci. Eng.* 165, 42–57.
- Väizene, V., Valgma, I., Karu, V., Orru, M., 2016. Environmental impact of oil shale mining. *Environm. Earth Sci.* 75, 1201.
- Wang, S., Dong, K., Feng, M., Huo, Y., 2013. Influence of perforation parameters on hydraulic fracture initiation. *J. Appl. Sci.* 13 (12), 2321–2325.
- Wang, T., Hu, W., Elsworth, D., Zhou, W., Zhou, W., Zhao, X., 2017. The effect of natural fractures on hydraulic fracturing propagation in coal seams. *J. Pet. Sci. Eng.* 150, 180–190.
- Wang, X., Shi, F., Liu, H., Wu, H., 2016. Numerical simulation of hydraulic fracturing in orthotropic formation based on the extended finite element method. *J. Nat. Gas Sci. Eng.* 33, 56–69.
- Wu, L., Tjahjanto, D., Becker, G., Makradi, A., Jérusalem, A., Noels, L., 2013. A micro-meso-model of intra-laminar fracture in fiber-reinforced composites based on a discontinuous Galerkin/cohesive zone method. *Eng. Fract. Mech.* 104, 162–183.
- Xie, J., Cheng, W., Wang, R., Jiang, G., Sun, D., Sun, J., 2018a. Experiments and analysis on the influence of perforation mode on hydraulic fracture geometry in shale formation. *J. Pet. Sci. Eng.* 168, 133–147.
- Xie, J., Huang, H., Ma, H., Zeng, B., Tang, J., Yu, W., Wu, K., 2018b. Numerical investigation of effect of natural fractures on hydraulic-fracture propagation in unconventional reservoirs. *J. Nat. Gas Sci. Eng.* 54, 143–153.
- Xie, L., Min, K.-B., Shen, B., 2016. Simulation of hydraulic fracturing and its interactions with a preexisting fracture using displacement discontinuity method. *J. Nat. Gas Sci. Eng.* 36, 1284–1294.
- Yang Hao, D.Y., 2014. A feasibility study on in-situ heating of oil shale with injection fluid in China. *J. Pet. Sci. Eng.* 122, 304–317.
- Yang, L., Chen, C., Jia, R., Sun, Y., Guo, W., Pan, D., Li, X., Chen, Y., 2018. Influence of reservoir stimulation on marine gas hydrate conversion efficiency in different accumulation conditions. *Energies* 11 (2), 339.
- Yao, Y., Liu, L., Keer, L.M., 2015. Pore pressure cohesive zone modeling of hydraulic fracture in quasi-brittle rocks. *Mech. Mater.* 83, 17–29.
- Yushi, Z., Shicheng, Z., Tong, Z., Xiang, Z., Tiankui, G., 2015. Experimental investigation into hydraulic fracture network propagation in gas shales using CT scanning technology. *Rock Mech. Rock Eng.* 49 (1), 33–45.
- Zhao, S., Sun, Y., Wang, H., Li, Q., Guo, W., 2019. Modeling and field-testing of fracturing fluid back-flow after acid fracturing in unconventional reservoirs. *J. Pet. Sci. Eng.* 176, 494–501.
- Zhao, X., Ju, Y., Yang, Y., Su, S., Gong, W., 2016. Impact of hydraulic perforation on fracture initiation and propagation in shale rocks. *Sci. China Technol. Sci.* 59 (5), 756–762.
- Zhou, J., Chen, M., Jin, Y., Zhang, G.-q., 2008. Analysis of fracture propagation behavior and fracture geometry using a tri-axial fracturing system in naturally fractured reservoirs. *Int. J. Rock Mech. Min. Sci.* 45, 1143–1152.
- Zhou, J., Jin, Y., Chen, M., 2010. Experimental investigation of hydraulic fracturing in random naturally fractured blocks. *Int. J. Rock Mech. Min. Sci.* 47, 1193–1199.